Energy Materials and Devices

Open Access
Research Article

Graphical Abstract

ZnAl-layered double hydroxides template-induced formation of ZnO/ZnSe heterostructures on the surface of coal-tar-pitch-derived carbon for high-efficiency sodium storage

Yibo Zhao[1], Peihua Li[2], Rufeng Tian[5], Haochen Xie[2], Yalong Wang[2], Wanggang Zhang[2], Xiaohong Li[5], Jian Wang[2] ✉, and Yiming Liu[1,3,4] ✉

[1] *College of Environmental Science and Engineering, Taiyuan University of Technology, Taiyuan 030024, China*
[2] *College of Materials Science and Engineering, Taiyuan University of Technology, Taiyuan 030024, China*
[3] *School of Chemical Engineering and Technology, Taiyuan University of Science and Technology, Taiyuan 030024, China*
[4] *Shanxi Key Laboratory of Catalysis and Energy Coupling, Taiyuan University of Science and Technology, Taiyuan 030024, China*
[5] *College of Chemistry and Chemical Engineering, Taiyuan University of Technology, Taiyuan 030024, China*

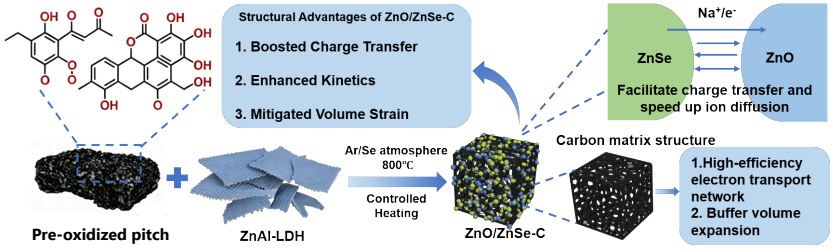

ZnO/ZnSe heterostructures are *in situ* grown on pitch-derived carbon using a zinc–aluminum layered double hydroxide (ZnAl-LDH) template to form a porous conductive composite, with high reversible capacity, excellent rate capability, and long-term cycling stability achieved in sodium-ion batteries.

✉ Address correspondence to
Jian Wang, wangjian@tyut.edu.cn;
Yiming Liu, liuym812@163.com

Received: January 9, 2026
Revised: April 16, 2026
Accepted: April 19, 2026

Read Online

Citation: Zhao Y., Li P., Tian R., et al. ZnAl-layered double hydroxides template-induced formation of ZnO/ZnSe heterostructures on the surface of coal-tar-pitch-derived carbon for high-efficiency sodium storage. *Energy Mater. Devices*, 2026, 4(2), 9370093. https://doi.org/10.26599/EMD.2026.9370093

Energy Materials and Devices
https://doi.org/10.26599/EMD.2026.9370093
Open Access
Research Article

ZnAl-layered double hydroxides template-induced formation of ZnO/ZnSe heterostructures on the surface of coal-tar-pitch-derived carbon for high-efficiency sodium storage

Yibo Zhao[1], Peihua Li[2], Rufeng Tian[5], Haochen Xie[2], Yalong Wang[2], Wanggang Zhang[2], Xiaohong Li[5], Jian Wang[2] ✉, and Yiming Liu[1,3,4] ✉

[1] *College of Environmental Science and Engineering, Taiyuan University of Technology, Taiyuan 030024, China*
[2] *College of Materials Science and Engineering, Taiyuan University of Technology, Taiyuan 030024, China*
[3] *School of Chemical Engineering and Technology, Taiyuan University of Science and Technology, Taiyuan 030024, China*
[4] *Shanxi Key Laboratory of Catalysis and Energy Coupling, Taiyuan University of Science and Technology, Taiyuan 030024, China*
[5] *College of Chemistry and Chemical Engineering, Taiyuan University of Technology, Taiyuan 030024, China*

Cite this article: *Energy Mater. Devices* 2026, **4**(2): 9370093. https://doi.org/10.26599/EMD.2026.9370093

ABSTRACT

Developing high-performance anodes from low-cost industrial byproducts is crucial for advancing sodium-ion batteries. Herein, we report a zinc–aluminum layered double hydroxide (ZnAl-LDH) template-induced strategy for fabricating ZnO/ZnSe heterojunctions embedded within hierarchical porous carbon derived from coal tar pitch. The LDH serves as a dual functional structural template and pore-forming agent, enabling the *in situ* construction of intimately coupled ZnO/ZnSe–C interfaces. The designed ZnO/ZnSe heterostructure offers notable advantages: the heterojunction boosts charge transfer via interfacial contact between the two active components, while the mixed O^{2-}/Se^{2-} anion environment, combined with nanodispersed ZnO/ZnSe and the conductive carbon matrix, effectively enhances the reaction kinetics and mitigates volume strain. Consequently, the composite anode delivers a high reversible capacity of 637.5 mAh g^{-1} at 100 mA g^{-1} and retains 259.7 mAh g^{-1} after 1000 cycles at 5 A g^{-1}. Kinetic analysis indicates that the superior rate performance is attributed to a dominant capacitive contribution (93.3% at 1.2 mV s^{-1}). A full cell configured with an $Na_3V_2(PO4)_3$ cathode demonstrates practical viability, retaining 147.5 mAh g^{-1} after 100 cycles. This work highlights the effectiveness of LDH-templated synthesis in constructing advanced heterostructure anodes for efficient sodium storage.

KEYWORDS

anode material, coal tar pitch, layered double hydroxide, heterostructure, ZnSe, sodium-ion battery

1 Introduction

Given the natural abundance and cost-effectiveness of sodium, the pursuit of sustainable energy storage has positioned sodium-ion batteries (SIBs) as promising alternatives to lithium-ion systems[1]. To achieve practical SIBs, developing high-performance anode materials is critical. Amorphous carbon derived from industrial byproduct pitch stands out as a compelling candidate because of its low cost, good conductivity, and structural tunability[2–4]. However, pristine pitch-derived carbons often suffer from limited interlayer spacing and underdeveloped pore structures, which inherently restrict the kinetics of Na^+ diffusion and achievable capacity[5].

In recent years, metal chalcogenides have attracted extensive attention as promising anode materials for SIBs owing to their abundant reserves, tunable electronic structures, and high theoretical specific capacities[6]. Among them, zinc oxide (ZnO) and zinc selenide (ZnSe) have earned distinction owing to their ultrahigh theoretical specific capacities (approximately 978 mAh g^{-1} and 820 mAh g^{-1}, respectively), which can effectively overcome the low-capacity limitation of traditional carbon-based anode materials[7]. Specifically, the intrinsic adsorption/desorption active sites on the surface of ZnO lead to a more significant surface capacitive contribution[8]. In contrast, the reaction of ZnSe is dominated by bulk diffusion. However, because of the lower electronegativity of Se compared to that of O, ZnSe exhibits superior electronic conductivity, a property that can optimize the charge-transfer efficiency[9]. The combination of ZnO and ZnSe can simultaneously enable fast surface reactions and provide sufficient bulk capacity because the mixed O^{2-}/Se^{2-} anion environment formed by their integration and the interfacial contact between the two components effectively optimizes the charge-transfer efficiency of the

Received: January 9, 2026 / **Revised:** April 16, 2026 / **Accepted:** April 19, 2026

✉ **Address correspondence to** Jian Wang, wangjian@tyut.edu.cn; Yiming Liu, liuym812@163.com

composite[10–12]. However, the practical application of these materials is hindered by inherent challenges, including severe volume expansion during cycling and poor intrinsic conductivity, which often lead to particle pulverization and rapid capacity decay. To address these issues, compositing with carbon matrices (e.g., graphene and porous carbon) has emerged as a mainstream strategy. This approach enhances electron transport by forming conductive networks and buffers volume changes by conferring structural flexibility. For example, a 3D-ordered hierarchical porous ZnSe@N-doped carbon composite was fabricated, which demonstrated outstanding cycling stability, retaining 241.6 mAh g^{-1} after 800 cycles at 10 A g^{-1} owing to the synergy between the porous structure and carbon support[13]. Further, a representative synthesis route involves the *in situ* transformation of zinc-based metal–organic frameworks (e.g., ZIF-8) into ZnO/ZnSe heterojunctions embedded in nitrogen-doped porous carbon skeletons. The morphology of such a structure is resistant to volume changes, while providing additional active sites through the porous carbon and heterojunction interfaces, thereby further enhancing the electrochemical performance[14].

The quest for such synergistic, carbon-integrated metal chalcogenide anodes has spurred the exploration of versatile precursor templates. Beyond the commonly used metal–organic frameworks (MOFs), layered double hydroxides (LDHs) have recently emerged as a superior class of sacrificial templates and reactive precursors for the design of advanced electrode materials, as evidenced by their successful deployment in high-performance cathodes and anodes for various metal-ion batteries[15]. The inherent merits of LDHs are multifaceted: their tunable bimetallic composition within the host layers facilitates the targeted synthesis of derived metal compounds (e.g., oxides), while the interlayer gallery can accommodate diverse anions, enabling precise chemical modification[16]. More importantly, in composites, the layered structure and the gases released (e.g., H_2O) during the thermal decomposition can effectively engineer the porosity and architecture of the associated carbon matrices[17]. This unique combination—acting as a metal source, a structure-directing agent, and an *in situ* pore-former—makes LDHs an exceptionally powerful template for constructing tightly coupled, heterostructured materials with optimized interfaces and conductive networks. Therefore, employing a rationally selected LDH as a template presents a compelling and potentially more versatile pathway than conventional routes for fabricating carbon–metal composites with enhanced sodium-storage capabilities.

Guided by the template functionality of LDHs, we propose a rational strategy for realizing the zinc–aluminum layered double hydroxide (ZnAl-LDH) template-induced formation of ZnO/ZnSe heterostructures on the surface of coal-tar-pitch-derived carbon. This is achieved through the preoxidation of pitch to form a composite precursor with ZnAl-LDH, followed by controlled carbonization and selenization. The derived material integrates multiple advantageous features: (i) the *in situ* decomposition of LDH generates gases that create a hierarchical porous carbon framework, enlarging the specific surface area and facilitating Na^+ transport[18]; (ii) the LDH-directed transformation yields uniformly dispersed ZnO/ZnSe heterojunctions with a mixed O^{2-}/Se^{2-} anion environment, and the interfacial contact between the two nanodispersed active components promotes charge transfer and accelerates the kinetics of ion diffusion; and (iii) the conductive and mechanically resilient carbon matrix not only buffers volume variation during cycling but also establishes continuous electron pathways[19]. Such rational design enables complementary contributions, wherein the ZnO/ZnSe active phases deliver high reversible capacity through conversion reactions, while the formed heterostructure effectively accelerates the reaction kinetics and improves the efficiency of active material utilization. Moreover, the porous carbon matrix enhances the surface-driven capacitive storage and structural stability. Consequently, the optimized composite exhibits outstanding sodium-storage performance, including high reversible capacity, remarkable rate capability, and long-term cycling durability in both half- and full-cell configurations.

2 Experimental section

2.1 Synthesis of materials

As illustrated in Fig. S1 in the Electronic Supplementary Material (ESM), the synthetic route consists of three main steps: preparation of ZnAl-LDH, preoxidation of coal tar pitch (to obtain comparison, the preoxidized pitch), and final fabrication of the composite material.

First, ZnAl-LDH was synthesized as follows: 1.09 g of zinc chloride ($ZnCl_2$), 0.75 g of aluminum chloride ($AlCl_3$), and 3 g of urea ($CO(NH_2)_2$) were weighed and dissolved in 100 mL of deionized water, followed by magnetic stirring for 30 min until complete dissolution. The resulting clear solution was transferred to a 150 mL Teflon-lined stainless steel autoclave and reacted at 120°C for 12 h. After the reaction system cooled naturally to room temperature, the white precipitate formed was collected, separated by centrifugation, washed thoroughly with deionized water and anhydrous ethanol several times, and finally dried in an oven at 60°C overnight.

Subsequently, the coal tar pitch was preoxidized by first grinding a lump of coal tar pitch into a fine powder, followed by and washing with deionized water to remove impurities. The pitch powder was then placed under an atmosphere of pure flowing oxygen, heated to 295°C at a rate of 2°C·min^{-1}, and held at this temperature for 10 h to complete the stabilization process, yielding preoxidized pitch, denoted as CTP.

Finally, the ZnO/ZnSe–C composites were fabricated: as-prepared ZnAl-LDH and CTP were physically mixed in different mass ratios (1:2, 1:1, and 2:1), dispersed in 50 mL of anhydrous ethanol, and sonicated for 1 h to form a homogeneous dispersion. The mixture was transferred to a vacuum-oven and dried at 80°C for 12 h to obtain the composite precursor. The precursor was then mixed with Se powder in a mass ratio of 1:2 and placed in a tube-furnace for thermal treatment under Ar atmosphere. The thermal treatment was programmed as follows: heat to 800°C at a rate of 5°C·min^{-1}, hold for 2 h to complete the carbonization and selenization reactions, and then cool

naturally to room temperature in the furnace. The resulting black product was washed with 100 mL of 0.1 mol·L^{-1} NaOH solution to remove residual Se powder and soluble Al-containing compounds, followed by drying at 80°C. Based on the initial mass ratios of ZnAl-LDH to CTP, the final samples were labeled as ZnO/ZnSe–C-1:2, ZnO/ZnSe–C-1:1, and ZnO/ZnSe–C-2:1, respectively.

In addition, for comparison, CTP was directly carbonized using the same process parameters (800°C, Ar atmosphere, holding for 2 h) without the addition of ZnAl-LDH and Se powder; the resulting product is designated as CTP–C.

2.2 Characterization of materials

The morphology and microstructure of the samples were characterized using field-emission scanning electron microscopy (FE-SEM; Tescan MIRA3 LMH) and transmission electron microscopy (TEM; JEOL JEM-2100F). Corresponding elemental mapping was performed using an energy-dispersive X-ray (EDX) spectroscopy attachment on the TEM. Crystal structures were analyzed by X-ray diffraction (XRD, Rigaku SmartLab) with Cu Kα radiation (λ = 0.15406 nm) in the 2θ range of 10°–80°. Raman spectra were recorded on a Renishaw Invia spectrometer using a 532 nm laser. The specific surface area and pore structure were determined by N_2 adsorption–desorption measurements at 77 K using a JW-BK-122W analyzer, where the specific surface area was calculated using the Brunauer-Emmett-Teller (BET) method and the pore size distribution was derived from the Barrett-Joyner-Halenda model. The surface chemical composition and valence states were investigated using X-ray photoelectron spectroscopy (XPS, Thermo Scientific Escalab 250Xi) with a monochromatic Al-Kα X-ray source (1486.6 eV). All binding energies were calibrated relative to the C 1s peak at 284.8 eV.

2.3 Evaluation of electrochemical performance

The working electrodes were prepared by mixing the active material, acetylene black, and polyvinylidene fluoride binder in a mass ratio of 7:2:1 in *N*-methyl-2-pyrrolidone to form a homogeneous slurry. The slurry was uniformly coated onto a copper foil current collector and dried at 120°C under vacuum for 12 h. The dried electrodes were then punched into disks with a diameter of 15 mm. The average mass loading of the active material was controlled at approximately 1.0–1.2 mg cm^{-2}.

For the half-cell tests, CR2032 coin cells were assembled in an argon-filled glove-box (H_2O < 0.1 ppm, O_2 < 0.1 ppm). Sodium metal foil was used as the counter/reference electrode, and a glass fiber membrane (Whatman GF/C) was used as the separator. The electrolyte comprised 1 mol/L $NaClO_4$ dissolved in a mixture of ethylene carbonate, dimethyl carbonate, and ethyl methyl carbonate (1:1:1 by volume), with 5 wt% fluoroethylene carbonate additive.

For the full-cell tests, $Na_3V_2(PO_4)_3$ (NVP) was used as the cathode. The NVP cathode was prepared by mixing NVP, acetylene black, and polyvinylidene fluoride in a mass ratio of 8:1:1. To balance the charge, the mass ratio of the cathode (NVP) to the anode (ZnO/ZnSe–C composite) was carefully controlled at approximately 1.05:1 based on the respective reversible capacities of each anode[20]. Prior to full-cell assembly, the ZnO/ZnSe–C anode was pre-cycled in a half-cell for 5 cycles in the range of 0.01–3.0 V to form a stable solid electrolyte interphase (SEI) and eliminate irreversible capacity.

Galvanostatic charge–discharge (GCD) tests were performed on a LAND CT2001A battery test system within the voltage windows of 0.01–3.0. V (half-cell) and 1.0–4.3 V (full cell) at various current densities. Cyclic voltammetry (CV) analyses were conducted on a CHI760E electrochemical workstation at scan rates from 0.2 to 1.2 mV s^{-1}. Electrochemical impedance spectroscopy (EIS) measurements were performed on the same workstation over the frequency range of 0.01–100 kHz, with an applied amplitude of 5 mV. The galvanostatic intermittent titration technique (GITT) was employed to determine the Na^+ diffusion coefficient. The cells were pulsed at a constant current (0.05 A g^{-1}) for 10 min, followed by open-circuit relaxation for 40 min until the potential stabilized.

In situ characterization was performed using specialized electrochemical cells. *In situ* electrochemical impedance spectroscopy was conducted during the charge/discharge processes using a three-electrode cell (Tianjin Aida Hengsheng Technology), whereas *in situ* Raman spectra were collected using a two-electrode optical cell (Tianjin Gaoss Union Photoelectric Technology).

3 Results and discussion

3.1 Morphology and structure of the as-prepared samples

The morphology and microstructure of Zn-LDH, CTP–C, and their composites were systematically investigated using SEM and TEM. As shown in Fig. 1a, pristine ZnAl-LDH comprises sphere-like aggregates composed of distinct lamellar sheets. In contrast, the directly carbonized pitch (CTP–C, Fig. 1b) displays a stacked lamellar structure with a relatively uniform morphology. The SEM images of the composite precursors with different LDH-to-CTP mass ratios (1:2, 1:1, and 2:1) are presented in Fig. 1c, Figs. S2a and S2b in the ESM. At a low LDH loading (ratio 1:2, Fig. S2a), the distribution of LDH on the surface of CTP is uneven, leaving parts of the carbon matrix exposed and resulting in a rough, bulky morphology. When the ratio is balanced at 1:1 (Fig. 1c), the composite forms agglomerated particles and a continuous porous network. Slight inhomogeneity is observed in the SEM image, attributed to the simple physical blending process and possible insufficient grinding or inadequate mixing time during precursor preparation. Nevertheless, the obtained hierarchical structure remains conducive to enhanced electron transport and efficient ion diffusion. However, at a high LDH ratio of 2:1 (Fig. S2b in the ESM), severe agglomeration occurs, the particle dispersibility deteriorates, and the pore structure becomes blocked. Further detailed microstructural analysis was performed using TEM. Figure 1d clearly shows heteroatomic particles dispersed within the carbon matrix. The corresponding EDX elemental mappings in Fig. 1e confirm the uniform distribution of C, O, Zn, and Se throughout the material, indicating a well-integrated composite. The high resolu-

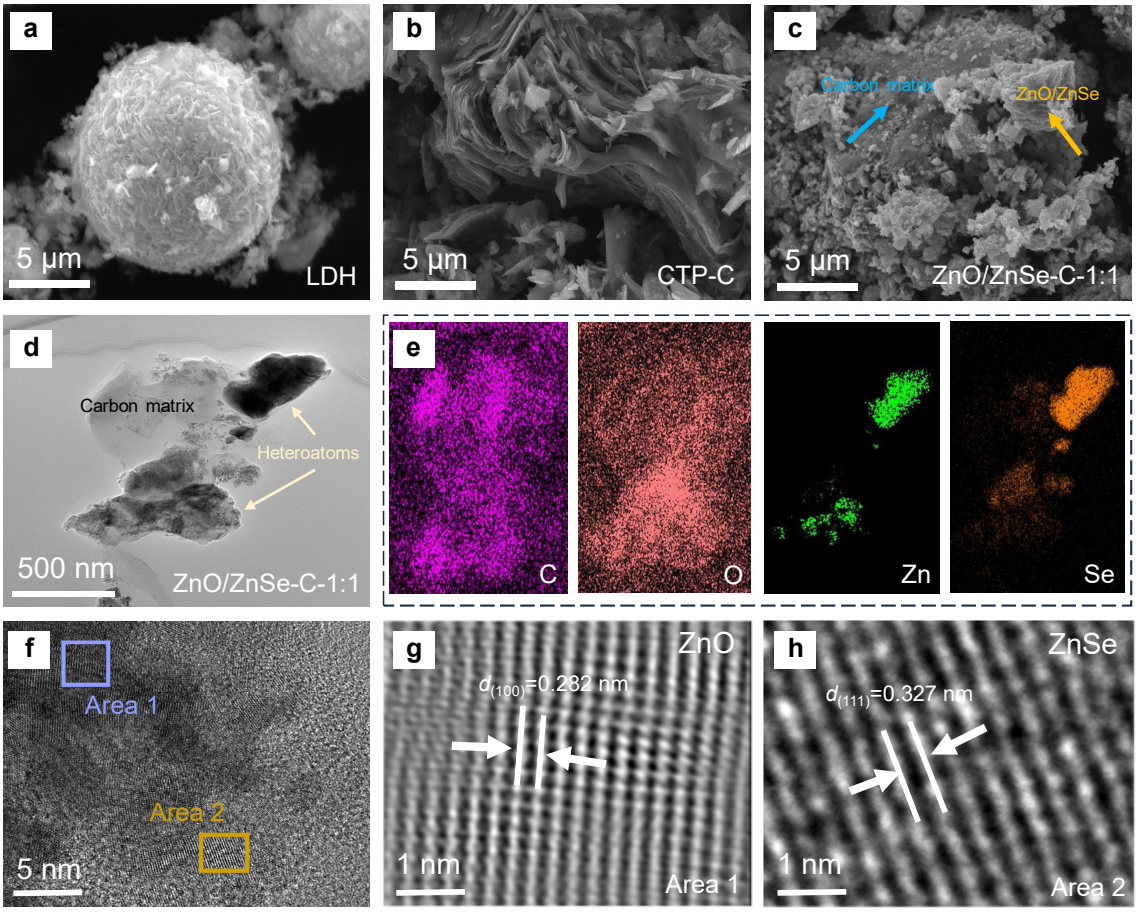

Figure 1 SEM images of LDH (a), CTP–C (b), and ZnO/ZnSe–C-1:1 (c). (d) TEM image of ZnO/ZnSe–C-1:1. (e) EDX mapping of ZnO/ZnSe–C-1:1. HR-TEM image (f) of ZnO/ZnSe–C-1:1 and correponding magnified region (g, h).

tion TEM (HR-TEM) image in Fig. 1f clearly shows two distinct crystalline regions, confirming the formation of a heterostructure. As displayed in the magnified lattice images (Figs. 1g and 1h), the measured interplanar spacings are 0.282 nm in Area 1 and 0.327 nm in Area 2, which is further supported by the lattice spacing profiles provided in Figs. S3a and S3b in the ESM. These values correspond to the (100) plane of ZnO (PDF#74-0534) and the (111) plane of ZnSe (PDF#37-1463), respectively.

Figure 2a presents the XRD patterns of the as-prepared sample. The XRD spectrum of CTP–C exhibits broad, diffuse peaks, a typical feature of amorphous carbon[21], confirming its predominantly disordered structure with low crystallinity. In contrast, the spectrum of pristine ZnAl-LDH displays sharp, well-defined diffraction peaks, consistent with its highly ordered, layered crystalline architecture. All composite samples show clear diffraction peaks corresponding to ZnO and ZnSe, indicating the transformation of LDH during high-temperature treatment and subsequent selenization. Notably, no residual peaks of Al-containing compounds or excess Se were observed after alkaline washing, confirming the effective removal of impurities. The Rietveld refinement profile (Fig. 2b) yields satisfactory reliability factors (R_p = 7.05% and R_{wp} = 9.60%). The elevated background primarily arises from diffuse scattering caused by long-range disordered graphitic domains in the pitch-derived carbon matrix. The refinement results indicate that ZnO constitutes approximately 15 wt% of the crystalline phase, demonstrating that under high-temperature carbonization and Se vapor, Zn-based species derived from LDH are efficiently and predominantly converted to ZnSe. This confirms that the introduced Se effectively promotes selenization, while subsequent alkaline washing does not compromise the primary ZnO/ZnSe heterostructure, thereby providing a controlled phase composition that supports sodium storage.

Raman spectra of the samples are shown in Fig. 2c. The D-band at 1336.4 cm^{-1} is associated with structural defects or sp^3-hybridized carbon, whereas the G-band at 1582.6 cm^{-1} corresponds to the in-plane vibration of sp^2-hybridized carbon[22]. The I_D/I_G ratio of CTP–C is 0.65, indicating only a small number of defects, which is consistent with the typical structural characteristics of preoxidized pitch-based carbon materials. With increasing LDH content in the composites, the I_D/I_G ratio gradually increased from 0.65 for CTP–C to 0.87 for ZnO/ZnSe–C-2:1. This trend can be ascribed to *in situ* pore formation induced by the gas released from LDH decomposition during carbonization, which destroys the partially graphitized domains of the carbon matrix and generates abundant pore edges and structural defects. In addition, the *in situ* anchored ZnO/ZnSe nanoparticles interact strongly with the carbon matrix, inhibiting graphitic ordering and increasing the structural disorder.

The nitrogen adsorption–desorption isotherms and pore-size distribution profiles are displayed in Fig. 2d[23].

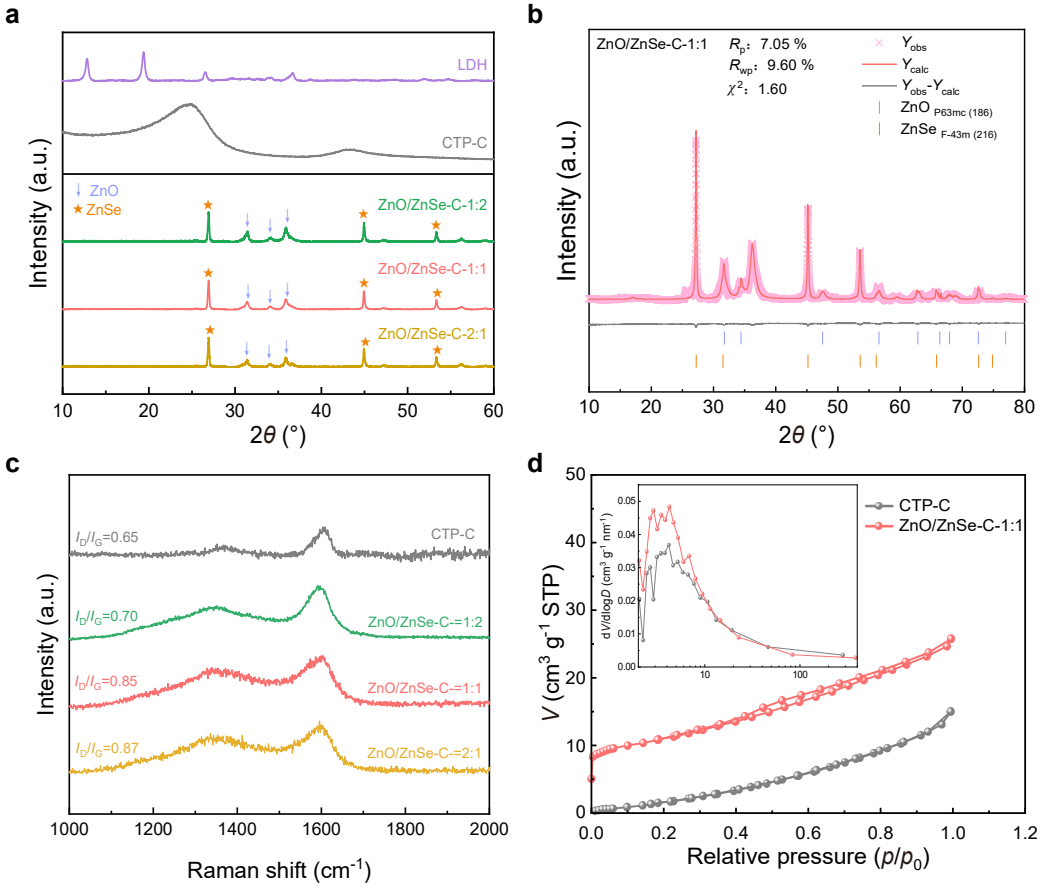

Figure 2 (a) XRD patterns of the samples. (b) Rietveld refinement of XRD pattern of ZnO/ZnSe–C-1:1. Raman spectrum (c) and BET curves (inset: pore size distribution) (d) of samples.

The isotherm of CTP–C is classified as Type IV, with limited adsorption capacity and no distinct hysteresis loop, indicating a poorly developed pore structure consisting mainly of slit-like mesopores between particles. The isotherm of the ZnO/ZnSe–C-1:1 composite is also Type IV but with significantly enhanced adsorption across the entire pressure range[24]. The steep uptake at low relative pressure suggests the presence of abundant micropores/mesopores, whereas the continuous adsorption at medium–high pressures, combined with the broad hysteresis loop, reflects a well-developed, mesoporous, slit-pore structure derived from the LDH precursor. These results confirm that the introduction of LDH substantially increases the specific surface area and pore volume of the composite.

XPS was used to characterize and analyze the distribution of heteroatomic functional groups in ZnO/ZnSe–C-1:1. The XPS survey spectrum of ZnO/ZnSe–C-1:1 is presented in Fig. S4 in the ESM. Figure 3a shows the deconvoluted peaks (and their respective binding energies) in the C 1s core-level spectrum. The C–C bond corresponds to a binding energy of 284.8 eV, while C–O bond gives rise to a signal at 285.6 eV; the C=O bond has an energy of 287.5 eV, and the π-π^* satellite peak appears at 289.2 eV[25]. The two distinct deconvoluted peaks in the O 1s spectrum (Fig. 3b) correspond to C=O (531.1 eV) and C–O (532.3 eV), respectively[26]. The Zn 2p core-level spectrum (Fig. 3c) exhibits two characteristic peaks of Zn $2p_{3/2}$ at 1022.1 eV and Zn $2p_{1/2}$ at 1045.1 eV[27]. Deconvolution of the Se 3d core-level spectrum (Fig. 3d) yields two peaks: Se $3d_{5/2}$ at 54.7 eV and Se $3d_{3/2}$ at 56.5 eV[28]. These analyses confirm that all components of ZnO/ZnSe–C-1:1 exist in their typical valence states, indicating that the composite possesses the expected chemical composition and bonding structure. Notably, C–O is more abundant than C=O because the oxygen-containing functional groups inherent in the preoxidized pitch are partially retained during high-temperature carbonization, while interfacial interactions between the LDH-derived metal oxides and carbon matrix further promote the formation and stabilization of C–O bonds[20].

3.2 Electrochemical performance in SIBs

The different materials and composites synthesized at various temperatures were used as anodes for SIBs, and their electrochemical performance was characterized and analyzed. Figure 4a presents the first three CV curves of ZnO/ZnSe–C-1:1 at a scan rate of 0.2 mV s^{-1}. The prominent peak at 0.99 V corresponds to the formation of the SEI film. The redox peaks at 0.94 and 0.65 V correspond to the redox reaction of ZnS[8]. A pair of small impurity peaks appear at 1.56 and 1.88 V, which may originate from the redox reactions induced by the low-content Zano phase[29]. Figure 4b shows the characteristic plateau in the voltage range of 0.5–1.0 V, which corresponds to the conversion reactions of ZnO and ZnSe, whereas the plateau below 0.2 V is attributed to the intercalation of Na^+ into the pseu-

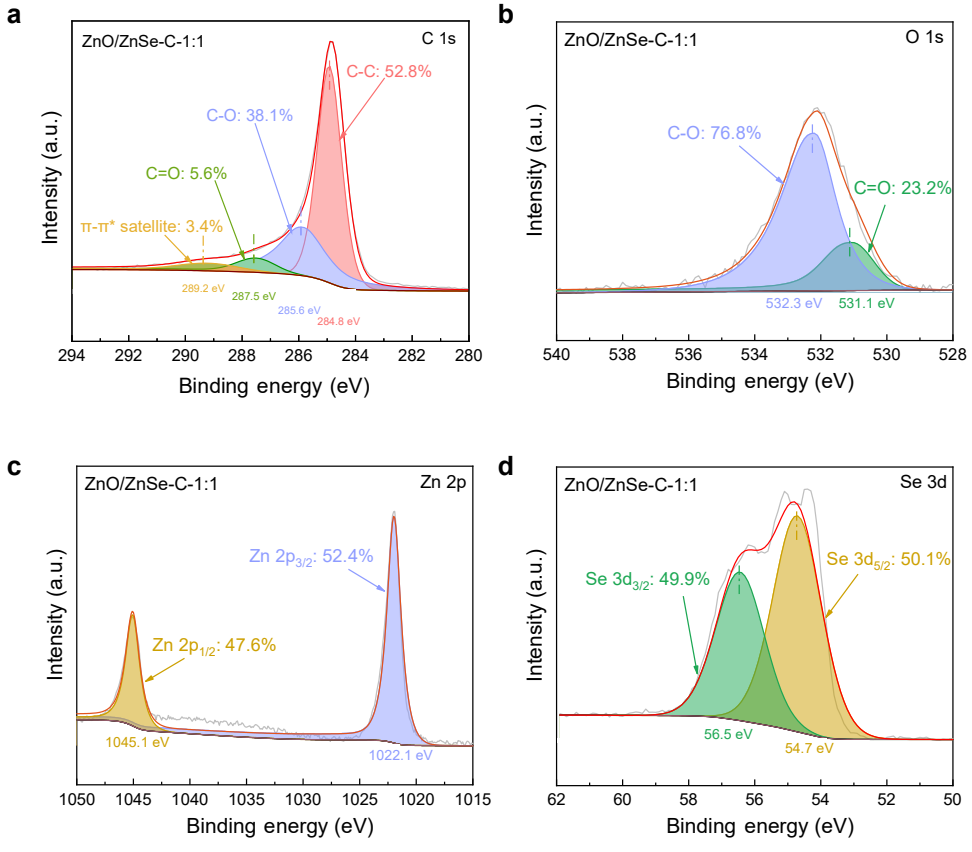

Figure 3 Fitted XPS C 1s (a), O 1s (b), Zn 2p (c), and Se 3d (d) curves of ZnO/ZnSe–C-1:1.

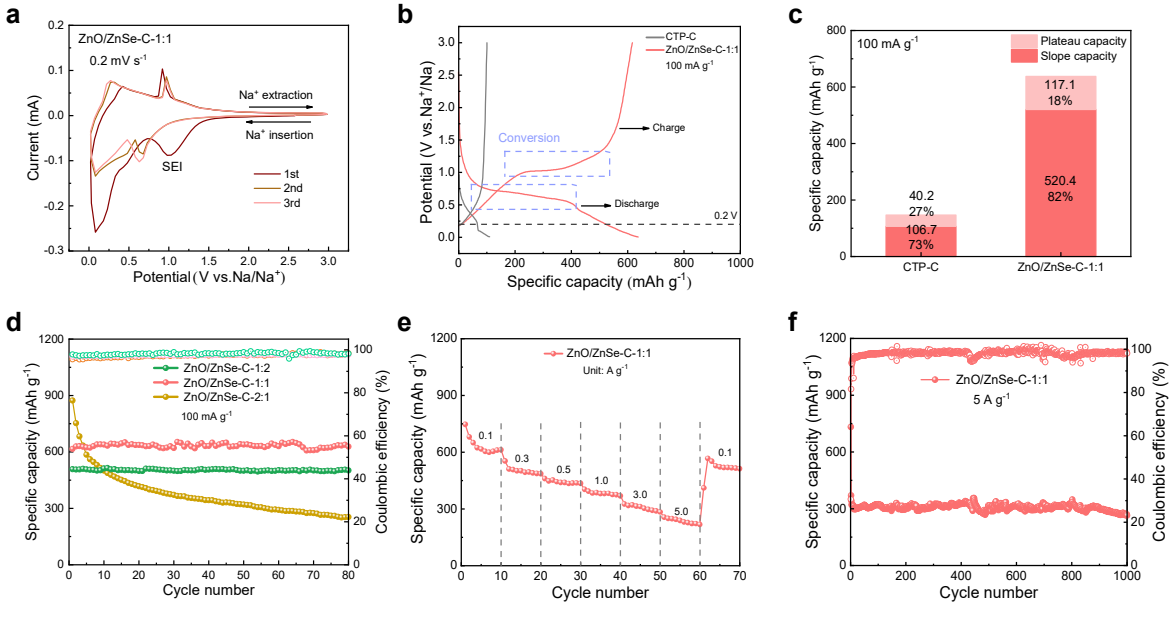

Figure 4 (a) CV curves of ZnO/ZnSe–C-1:1. GCD curves (b) and capacity contribution (c) of CTP–C and ZnO/ZnSe–C-1:1 in the second cycle discharge at 100 mA g^{-1}. (d) Cycling performance at 100 mA g^{-1}. (e) Rate performance. (f) Long-term cycling performance at 5 A g^{-1}.

dographitic layers of pitch-derived carbon. To further verify this assignment, the CV curve of pure CTP–C is provided in Fig. S5 in the ESM. The results show a distinct reduction peak in the low-potential region below 0.2 V for pure CTP–C, which corresponds to the intercalation of Na^+ into the pseudo-graphitic structure of pitch-derived carbon, directly confirming the origin of the low-potential sodium intercalation signal in the spectrum of the composite electrode. Note that no obvious low-potential plateau is present in the charge–discharge profile of pure CTP–C, which is an inherent electrochemical characteristic of pitch-based soft carbon. The sodium-storage

behavior is largely manifested as a sloping profile rather than a distinct plateau, but this does not indicate the absence of sodium intercalation in this potential region. In contrast, the CV curves exhibit higher sensitivity toward weak redox signals, enabling accurate detection of the low-potential sodium intercalation behavior, thereby fully validating the rationality of assigning the low-potential plateau of the composite electrode to sodium intercalation into the carbon layers. The processes are described by Eqs. 1–6[8,29]:

Discharge process:

$$6C + xNa^+ + xe^- \rightarrow Na_xC_6 \quad (1)$$

$$ZnO + 2Na^+ + 2e^- \rightarrow Zn + Na_2O \quad (2)$$

$$ZnSe + 2Na^+ + 2e^- \rightarrow Zn + Na_2Se \quad (3)$$

Charge process:

$$6C + xNa^+ + xe^- \rightarrow Na_xC_6 \quad (4)$$

$$Zn + Na_2O \rightarrow ZnO + 2Na^+ + 2e^- \quad (5)$$

$$Zn + Na_2Se \rightarrow ZnSe + 2Na^+ + 2e^- \quad (6)$$

As shown in Fig. 4c, compared with CTP–C, ZnO/ZnSe–C-1:1 not only achieves a significant capacity increase but also exhibits a notable increase in its capacitive contribution ratio. This stems from the dual sodium storage enhancement introduced by the conversion reaction: on one hand, the reversible conversion reaction between ZnO/ZnSe and Na^+ provides a large number of additional sodium storage active sites, directly boosting the total sodium-storage capacity of the material; on the other hand, the surface and near-surface charge-transfer processes involved in the conversion reaction are kinetically fast[30]. Coupled with the well-developed hierarchical pore structure of the composite and the efficient ion–electron transport channels formed at the heterointerface, this significantly enhances the capacitive sodium storage, thereby leading to a marked increase in the capacitive contribution ratio. As shown in Fig. 4d, Figs. S6 and S7 in the ESM, the CTP–C, ZnO–C, and ZnAl-LDH–C anode materials deliver reversible specific capacities of 112.3, 178.7, and 311.2 mAh·g^{-1}, respectively, at a current density of 100 mA·g^{-1}. In contrast, the pitch-based carbon material loaded with the heterostructures (ZnO/ZnSe–C-1:1) achieves a specific capacity of 637.5 mAh·g^{-1} under identical test conditions, thus exhibiting superior electrochemical performance. As shown in Fig. 4e, ZnO/ZnSe–C-1:1 delivers capacities of 680.9, 511.1, 460.4, 393.3, 321.1, and 248.6 mAh g^{-1} at current densities of 0.1, 0.3, 0.5, 1.0, 3.0, and 5.0 A g^{-1}, respectively, demonstrating excellent rate capability. Notably, as shown in Fig. 4f, after 1000 cycles at a high current density of 5.0 A g^{-1}, ZnO/ZnSe–C-1:1 still retains a reversible capacity of 259.7 mAh g^{-1}, showing outstanding cycle life. Comparative evaluation of the heterostructure-loaded anodes in SIB half-cells demonstrates that ZnO/ZnSe–C maintains excellent capacity across a broad range of current densities (Table S1 in the ESM)[31–36]. The significantly enhanced surface capacitive effect corresponds to rapid ion transfer and is the origin of the outstanding rate performance of ZnO/ZnSe–C-1:1 at high current densities.

To investigate the Na^+ storage behavior of ZnO/ZnSe–C-1:1, CV curves were recorded at scan rates ranging from 0.2 to 1.2 mV s^{-1}, as presented in Fig. 5a. As the scan rate increases, the area of the corresponding CV curve gradually expands. The relationship between the peak current (i) and scan rate (v) can be quantified using Eqs. 7 and 8[37]:

$$i = av^b \quad (7)$$

$$\log i = b \log v + \log a \quad (8)$$

The b-value is an indicator of the electrochemical energy storage characteristics during redox processes. The b-values cluster within the range of 0.5–1.0, indicating that sodium storage involves the combined effects of surface capacitive behavior and bulk ion diffusion[38]. The b-values of the anodic peaks are smaller than those of the cathodic peaks, which means that the kinetics of the anodic reactions tend to be dominated by bulk ion diffusion, possibly owing to the higher diffusion barrier that Na^+ has to overcome for deintercalation from the interior of the material. Notably, the b-values corresponding to the redox peaks of ZnO are more intense than those of ZnSe (Fig. 5b), indicating that the active sites formed by ZnO on the surface of the carbon matrix facilitate surface adsorption/desorption processes. In contrast, during the reaction of ZnSe, Na^+ needs to enter the interior of the lattice to participate in the conversion reaction; thus, the bulk diffusion step has a more pronounced influence on the reaction kinetics. Consequently, the b-values associated with the redox peaks of ZnSe are lower, indicating more prominent diffusion-controlled characteristics. The surface capacitance can be quantified using Eq. 9:

$$i = k_1 v + k_2 v^{1/2} \quad (9)$$

where k_1, k_2, and k_1v, and $k_2v^{1/2}$ represent the ratio of the surface capacitance and bulk ion diffusion, respectively[39]. As shown in Figs. 5c and 5d, the capacitive contribution ratio of ZnO/ZnSe–C-1:1 increases from 71.8% at 0.2 mV s^{-1} to 93.3% at 1.2 mV s^{-1}, while the corresponding diffusion contribution decreases from 28.2% to 6.7%. The above data clearly demonstrate that the proportion of the surface capacitive contribution gradually increases with increasing scan rate, while the proportion of the bulk diffusion contribution decreases accordingly. At low scan rates (≤0.6 mV s^{-1}), the bulk diffusion contribution (19.0%–28.2%) boosts the total capacity, which is consistent with the sodium-storage mechanism involving the conversion reaction of ZnO/ZnSe and Na^+ intercalation into the carbon layers. At high scan rates (≥1.0 mV s^{-1}), the surface capacitive contribution becomes dominant (≥ 88.5%), which is the key to the excellent rate performance of the composite: the surface adsorption/desorption process shows faster kinetics and is less limited by Na^+ diffusion.

To investigate the surface diffusion of Na^+, GITT measurements were performed on the SIBs, with a 10 min pulse period and a 10 min relaxation period. The Na^+ diffusion coefficient (D_{Na^+}) can be calculated using Eq. 10:

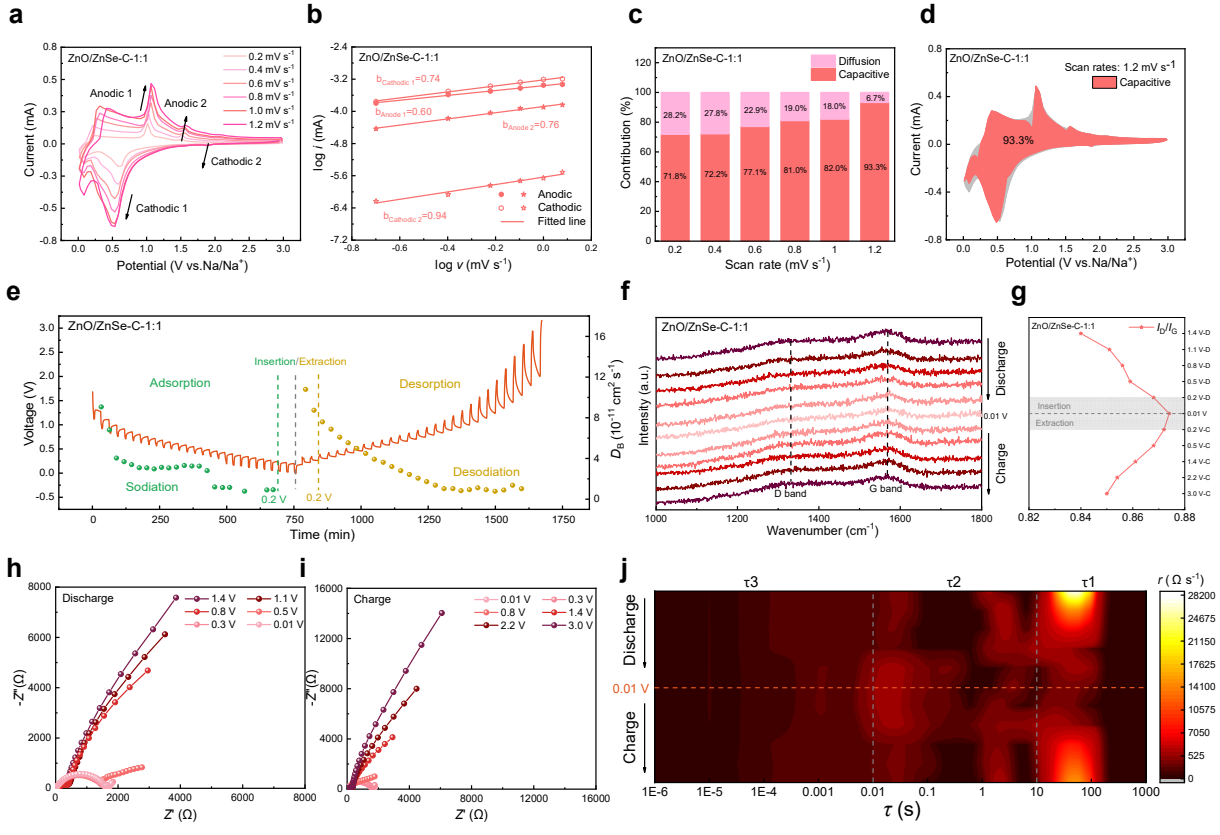

Figure 5 CV curves from 0.2 mV s^{-1} to 1.2 mV s^{-1} (a), *b*-values (b), ratio of capacitive contribution (c), capacitive contribution at 1.2 mV s^{-1} (d), and GITT profiles (e) of ZnO/ZnSe–C-1:1. *In situ* Raman spectrum (f) and corresponding I_D/I_G ratios (g) of ZnO/ZnSe–C-1:1. *In situ* EIS curves during discharge (h) and charge (i). (j) Contour plot of distribution of relaxation times for ZnO/ZnSe–C-1:1.

$$D_{Na^+} = \frac{4}{\pi\tau}\left(\frac{m_B V_M}{S M_B}\right)^2\left(\frac{\Delta E_s}{\Delta E_\tau}\right)^2 \quad (10)$$

Here, τ denotes the relaxation time (s); m_B represents the active mass (g); V_M indicates the molar volume (cm^3 mol^{-1}); S is the active surface area (cm^2); M_B is the molar mass (g mol^{-1}); ΔE_s is the change in the steady-state potential induced by the current pulse; and ΔE_τ is the potential change during this pulse after subtracting the *iR* drop[40]. As shown in Fig. 5e, the variation in the diffusion coefficient indicates that during discharge, as the potential decreases, the charge-transfer resistance increases and bulk diffusion slows down. In contrast, during charging, the Na^+ diffusion rate is initially high and then declines significantly. This behavior indicates that Na^+ diffusion is closely related to the ion insertion/extraction pathways and dynamic structural changes in the material. During discharge, continuous Na^+ insertion can induce local lattice distortion, narrowing the bulk diffusion channels and increasing the charge-transfer resistance, while slowing diffusion. In the early charging stage, Na^+ is mainly deintercalated from surface and near-surface active sites, where the diffusion rate is maximal owing to the shorter diffusion paths and lower interfacial resistance. As charging proceeds, Na^+ must migrate from deeper bulk regions to achieve complete deintercalation; moreover, lattice relaxation owing to prior Na^+ insertion may remain incomplete in some areas, further raising the energy barrier for ion diffusion[41]. This phenomenon confirms that the sodium-storage kinetics of the ZnO/ZnSe–C-1:1 composite are synergistically regulated by ion migration pathways and the structural response of the material, providing a kinetic-level explanation of the performance variations observed during the charge/discharge processes.

To further elucidate the Na^+ diffusion behavior in different voltage regions and its correlation with battery performance, the discharge process was divided into high-voltage (3.0–0.2 V) and low-voltage (0.2–0.01 V) regions for detailed analysis based on the GITT data in Fig. 5e. In the high-voltage region of 3.0–0.2 V, the Na^+ diffusion coefficient remains at a relatively high level, ranging from 1.8×10^{-11} to 12×10^{-11} cm^2 s^{-1}. This is attributed to the dominant sodium-storage behavior in this stage, including surface adsorption/desorption and the conversion reactions of ZnO/ZnSe, characterized by fast kinetics and short Na^+ diffusion paths. In contrast, the Na^+ diffusion coefficient drops sharply in the low-voltage region of 0.2–0.01 V, decreasing from 1.2×10^{-11} to 2.5×10^{-11} cm^2 s^{-1}. The main reason is that sodium storage in this stage is dominated by Na^+ intercalation into the carbon layers, where Na^+ must diffuse into the interior of the carbon matrix; additionally, continuous Na^+ intercalation induces local lattice distortion of the carbon matrix, narrowing the diffusion channels and further reducing the diffusion coefficient. The Na^+ diffusion behavior in different voltage regions exerts distinct effects on the electrochemical performance of the composite: the relatively high Na^+ diffusion coefficient in the high-voltage region ensures excellent rate performance of the composite at high current densities because the surface-dominated reactions can rapidly respond to

fast charge/discharge under high current densities. The low Na^+ diffusion coefficient in the low-voltage region is the main cause of the slight capacity attenuation at an ultrahigh current density of 10 A g^{-1}, while its influence is limited because this region only contributes 18% of the total discharge capacity.

In situ characterization is critical for resolving the dynamic structural evolution of electrode materials during electrochemical processes. *In situ* Raman spectroscopy offers real-time insights into the microstructural changes in the carbon matrix of the ZnO/ZnSe–C-1:1 electrode. Figure 5f presents *in situ* Raman spectra acquired at different potentials over one full charge–discharge cycle; the corresponding evolution of the I_D/I_G ratio is summarized in Fig. 5g. After completing one cycle, the I_D/I_G ratio largely reverts to its precycle value, indicating that structural evolution of the carbon matrix during sodium storage is dominated by reversible reconstruction. This endows the matrix with excellent structural stability, which provides crucial microstructural underpinning for ensuring long-term cycling performance of the electrode. During discharge, the I_D/I_G ratio gradually increases, peaking for the fully discharged state. This finding reveals that continuous Na^+ intercalation during discharge induces localized structural reconstruction of the carbon matrix, generating additional defect sites and disordered domains. These newly formed disordered domains act as supplementary Na^+ storage sites, directly contributing to enhancing the sodium-storage capacity. Conversely, during charging, the I_D/I_G ratio gradually decreases, indicating that Na^+ deintercalation is accompanied by reversible relaxation of the disordered structures of the carbon matrix, with some defect sites reverting to their original ordered states when Na^+ is desorbed, further confirming the structural reversibility of sodium storage in the carbon matrix.

Subsequently, *in situ* EIS measurements were performed on ZnO/ZnSe–C-1:1, and the corresponding distribution of relaxation times curves was derived via fitting. The results are presented in Fig. 5j, Figs. S8a and S8b in the ESM. Here, τ1 (>10 s) corresponds to the bulk Na^+ diffusion within the electrode, τ2 (0.01–10 s) to the charge-transfer process at the electrode/electrolyte interface, and τ3 (<0.01 s) to Na^+ migration in the electrolyte[42]. During cycling, as the potential decreases during discharge, the peak position in the τ1 region gradually decreases, whereas that in the τ2 region follows the opposite trend. This indicates that continuous Na^+ insertion during discharge triggers internal structural reconstruction of the electrode, shortening the characteristic relaxation time of the bulk diffusion process. Meanwhile, at the electrode/electrolyte interface, Na^+ enrichment and local charge accumulation prolong the relaxation time of the charge-transfer process; thus, the kinetics of the bulk diffusion and interfacial processes exhibit potential-dependent inverse regulation. As the potential increases, the trends in these two regions reverse relative to those during discharge, corresponding to Na^+ extraction during charging. The diffusion pathways within the electrode undergo reversible structural relaxation with Na^+ extraction, causing the characteristic relaxation time for bulk diffusion to recover. Simultaneously, Na^+ desorption at the interface improves the charge-transfer environment, shortening the relaxation time. This demonstrates the reversible kinetic response of the electrode. During discharge, the peak position of τ3 changes relatively little, indicating that Na^+ migration in the electrolyte is weakly affected by the discharge potential[43]. The electrolyte system maintains stable ion-transport capability during discharge, which serves as one of the key factors underpinning the stable electrochemical performance of the electrode.

The sodium-storage process in the ZnO/ZnSe–C-1:1 composite during discharge can be divided into three consecutive stages based on the potential range. In the high-potential region (3.0–0.5 V vs. Na^+/Na), interfacial capacitive adsorption and initial formation of the solid electrolyte interphase film are dominant. Na^+ is preferentially adsorbed on the surface of the ZnO/ZnSe heterostructures and oxygen-containing functional groups (C–O, C=O) of the carbon matrix to form a capacitive electric double-layer, while the electrolyte undergoes slight reduction to generate an initial SEI film containing C–O–Na and C=O (corresponding to the irreversible peak at 0.99 V in the CV curve, Fig. 4a). During this stage, the lattice structure of ZnO/ZnSe remains intact (XRD refinement confirms that ZnO accounts for 15 wt% of the crystalline phase, Fig. 2b). In the medium-potential region (0.5–0.2 V vs. Na^+/Na), reversible conversion reactions of ZnO and ZnSe occur (Eqs. 2 and 3). The (220) crystal plane of ZnO (d = 0.282 nm) and (111) crystal plane of ZnSe (d = 0.327 nm) gradually vanish, producing highly dispersed elemental Zn nanograins, as well as amorphous Na_2O and Na_2Se. These reactions correspond to the redox peaks of ZnSe (0.94 V, 0.65 V) and ZnO (1.56 V, 1.88 V) in the CV curve (Fig. 4a) and the distinct plateau in the 0.5–1.0 range. The voltage range of the GCD curve contributes a capacity of 117.1 mAh g^{-1} (accounting for 18% of the total capacity, Fig. 5b). The HR-TEM and XPS results confirm consumption of the ZnO/ZnSe crystalline phases (Figs.1f–1h, 3c and 3d). In the low-potential region (0.2–0.01 V vs. Na^+/Na), the synergistic effect of intercalation into the carbon matrix and alloying with Zn prevail. Na^+ is inserted into the pseudographitic interlayers of coal-tar-pitch-derived carbon (Eq. 1), and elemental Zn reacts with Na^+ to form a $NaZn_x$ alloy. The slope segment below 0.2 V in the GCD curve contributes 520.4 mAh g^{-1} (accounting for 82% of the total capacity, Fig. 4b). GITT tests indicate that the Na^+ diffusion coefficient in this region is 10^{-10} to 10^{-11} cm^2 s^{-1} (Fig. 5e), and *in situ* Raman spectroscopy confirms that Na^+ intercalation leads to increased defects in the carbon matrix (the I_D/I_G ratio increased to ~0.88, Figs. 5f and 5g).

The morphological changes of the material after cycling at a high current density were observed using SEM (Fig. S9 in the ESM). Prior to cycling, the electrode maintained a relatively intact morphology. After long-term cycling, the active material particles were slightly pulverized without obvious structural collapse, while the electrochemical performance of the electrode remained relatively stable. The core reason lies in the synergistic effect between ZnO/ZnSe and pitch-derived carbon. The flexible porous carbon framework buffers the volume expansion of ZnO/ZnSe, inhibits particle fragmentation and agglomeration, and forms a highly conductive network for efficient

charge transport at high current. In addition, it promotes the formation of a stable SEI and reduces side reactions. As a result, stable structure and performance are simultaneously achieved during high-rate cycling.

To gain deep insight into the mechanism underlying the cycling stability of the ZnO/ZnSe–C-1:1 anode, the electrode was subjected to Ar^+ etching XPS depth profiling after 1000 long-term cycles, providing direct evidence of the excellent stability and structural integrity of the SEI layer without obvious degradation or destruction. This technique provides depth-resolved chemical information from the electrolyte–electrode interface (etching time = 0 s) to the bulk region of the active material (etching time = 100 s, corresponding to about 1000 sputtering cycles). At the initial surface (0 s), the survey spectrum (Fig. 6a) is dominated by C 1s, O 1s, and Na 1s signals, confirming that the active material is covered by an intact SEI film composed mainly of C, O, Na, and Cl. As the etching time increases, the atomic ratios of C (~50%→38%) and O (~39%→34%) decrease while Na content increases sharply from ~8% to ~21%, and Cl species remain at a low level throughout the process. (Fig. 6b). These variations demonstrate the gradual removal of the organic-rich outer SEI layer upon continuous ion etching, accompanied by progressive penetration into the underlying electrode bulk of ZnO/ZnSe-C. This rapid penetration indirectly demonstrates the extremely low physical thickness of the SEI, which is critical for supporting the material-dominant capacitive sodium-storage behavior and high-rate performance.

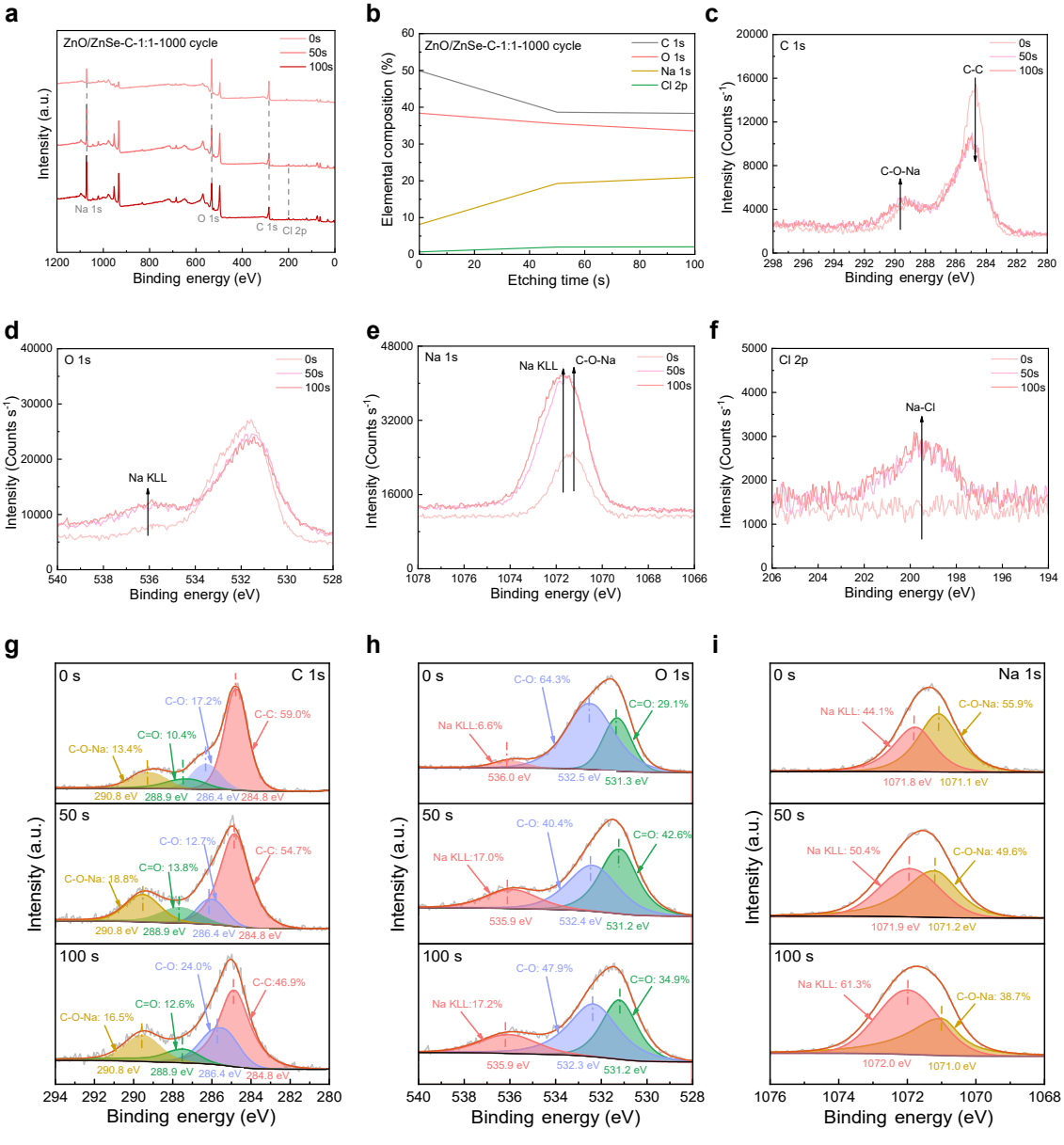

Figure 6 Characterization results for the ZnO/ZnSe–C-1:1 sample after 1000 cycles. (a) Survey XPS profiles as a function of etching time. (b) Variation in atomic percentages of key elements (C, O, Na, and Cl) with etching time. Original high-resolution C 1s (c), O 1s (d), Na 1s (e), and Cl 2p (f) XPS profiles at different etching depths. Deconvoluted high-resolution C 1s (g), O 1s (h), and Na 1s (i) XPS profiles as a function of etching depth.

Deconvolution of the high-resolution spectra enables depth-resolved mapping of the chemical composition of the SEI and verifies its typical "outer organic/inner inorganic" layered architecture. In the organic outer layer (0 s), the C 1s spectrum (Fig. 6c) is dominated by organic sodium salts (C–O–Na at 290.8 eV) and carbonate derivatives (C=O at 288.9 eV), verifying that this layer originates from electrolyte reduction products. The rapid attenuation of the O 1s peak intensity from the surface inward (Fig. 6d) further confirms that the SEI outer layer is primarily composed of oxygen-rich organic carbonates[44]. The macroscopic elemental profile (Fig. 6e) provides clear visualization of this bilayer structure. Notably, the atomic percentage of Na remains highly uniform (~10 at%) across all etching depths, providing direct evidence of the excellent mechanical robustness of the SEI, which effectively buffers the volume strain induced by the ZnSe conversion reactions. Moreover, the Cl 2p spectrum (Fig. 6f) shows that Na–Cl species are confined to the top surface and disappear rapidly by 50 s, and no obvious $NaClO_4$ signal is detected, indicating that the inner SEI layer effectively isolates the electrolyte from the active material and suppresses continuous side reactions[45].

The inorganic inner layer (50 and 100 s) in the SEI undergoes a distinct chemical transition with increasing etching depth. The characteristic peak positions and relative proportions of the main SEI components (C–C, C–O, C=O, C–O–Na) in the C 1s spectrum remain stable during long-term cycling, with C–C (stable carbon matrix) accounting for 59.0%–46.9% and C–O–Na (organic SEI component) varying slightly from 13.4% to 16.5%, suggesting no severe decomposition of the organic SEI. The significant increase in the C=O proportion (Fig. 6g) suggests dynamic decomposition and reconstruction of the SEI during long-term cycling, with continuous accumulation of carbonyl-containing organic components[46]. In the O 1s spectrum (Fig. 6h), the characteristic peaks and relative proportions of inorganic (Na–KLL, Na_2O) and organic (C=O, C–O) moieties remain intact, and the proportion of inorganic Na–KLL increases from 6.6% to 17.2% with the etching depth. Correspondingly, the Na 1s spectrum (Fig. 6i) shows a pronounced increase in the Na–KLL Auger peak (1072.6 eV, inorganic species) from 44.1% to 61.3% at 100 s, accompanied by a moderate decrease in the organic C–O–Na[47]. This inorganic-rich inner layer, containing Na_2O and Na_2Se from conversion reactions, provides rigid mechanical support and ensures the long-term chemical stability of the SEI. Ultimately, this ultrathin yet mechanically robust inorganic inner SEI lays the fundamental chemical foundation for fast Na^+ transport kinetics and contributes to the ultralong cycle life of the electrode at 5 A g^{-1}.

The comprehensive electrochemical performance of ZnO/ZnSe–C-1:1 as an anode was evaluated in a SIB full-cell system, with NVP as the cathode, having a high-voltage plateau[48]. Following the capacity balance principle, the mass ratio of active materials between the anode and cathode was set to 1.05:1. Prior to full-cell assembly, three complete cycles were performed at 30 mA g^{-1} to facilitate the formation of a stable SEI film on the anode. Figure 7a presents the GCD curves of the anode, cathode, and assembled full-cell, respectively. Figure 7b shows that the full-cell retains a reversible capacity of 147.5 mAh g^{-1} after 100 cycles at a current density of 100 mA g^{-1}. This demonstrates that the full-cell exhibits excellent long-term cycling stability. The stable SEI film formed during the pre-cycling process effectively suppresses structural degradation of the electrode materials and irreversible loss of the active components, thereby maintaining stable capacity retention after prolonged cycling. Figure 7c illustrates the rate capability of the ZnO/ZnSe–C-1:1//NVP full-cell, which delivers specific capacities of 258.2, 223.8, 192.4, 160.5, 126.7, and 109.9 mAh g^{-1} at current densities of 0.1, 0.3, 0.5, 1.0, 3.0, and 5.0 A g^{-1}, respectively. This performance reflects excellent rate adaptability. When the current density is increased from 0.1 A g^{-1} to 5.0 A g^{-1}, the capacity retention rate still reaches 42.6%. This indicates that the full-cell maintains satisfactory capacity retention even at high current densities. Figure 7d intuitively illustrates the layered structure and Na^+ transport mechanism in the ZnO/ZnSe–C//NVP sodium-ion full cell. The full cell comprises a copper foil current collector, ZnO/ZnSe–C anode, porous separator, NVP cathode, and aluminum foil current collector in a top-to-bottom sequence. During the discharge process, Na^+ ions are released from the ZnO/ZnSe–C anode, migrate through the separator to the NVP cathode, and are intercalated into the cathode lattice, while electrons are transported synchronously through the external circuit to complete the discharge reaction. The charge process proceeds in the reverse manner: Na^+ ions are deintercalated from the NVP cathode, flow back through the separator to the ZnO/ZnSe–C anode, and recombine with the anode material, enabling the reversible storage of sodium ions. This typical "rocking-chair" Na^+ transport behavior ensures efficient ion/electron transfer, providing a fundamental guarantee of the excellent rate capability and long-term cycling stability of the assembled full cell.

Furthermore, as shown in Fig. 7e, the battery retains a reversible specific capacity of 73.96 mAh g^{-1} after 70 cycles at a high current density of 3 A g^{-1}. This demonstrates that the full-cell exhibits excellent high-rate, long-term cycling stability. Figure 7f demonstrates the practical battery application. The full-cell can successfully drive a green light-emitting diode (LED) dot-matrix display to stably show the characters "TYUT", demonstrating the practical power-supply capability and application potential of the as-prepared ZnO/ZnSe–C anode material in sodium-ion full-cell devices.

4 Conclusion

In summary, we successfully developed a high-performance anode material for SIBs by loading layered double hydroxides onto preoxidized coal tar pitch, followed by vapor selenization. During the high-temperature process, ZnO derived from LDH decomposition and ZnSe from selenization form heterostructures that are anchored on the surface of the coal-tar-pitch-derived carbon matrix. This structure profoundly modulates the microstructure and surface chemical environment of the material, thereby enhancing its rate performance at high current densities. The ZnO/ZnSe–C-1:1 composite exhibits excellent electrochemical properties, delivering a specific capacity of 637.5 mAh g^{-1} at a current density of 100 mA g^{-1}, and retaining a high capacity of 259.7 mAh g^{-1} even at a high current density of 5 A g^{-1}. This remarkable performance

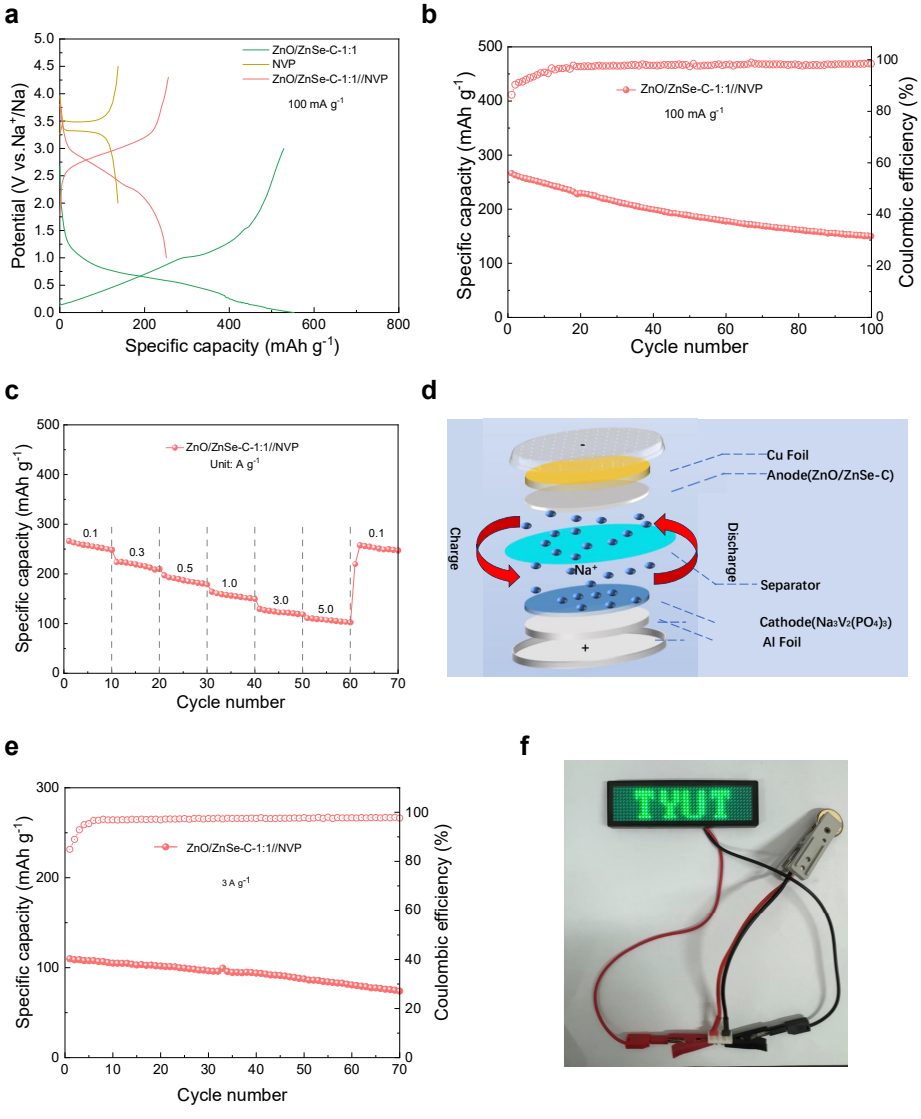

Figure 7 GCD curves (a), cycling performance (b), and rate performance (c) of ZnO/ZnSe–C-1:1//NVP. (d) Schematic of SIBs. (e) Cycling performance of ZnO/ZnSe–C-1:1//NVP at a high current density of 3 A g^{-1}. (f) Practical application of ZnO/ZnSe–C//NVP full cell for driving LED display.

stems from the outstanding capacitive contribution, which reaches 93.3% at a scan rate of 1.2 mV s^{-1}. The SIB full cell assembled with this anode and the compatible NVP cathode maintains a considerable reversible capacity of 147.5 mAh g^{-1} after 100 cycles at 100 mA g^{-1}, highlighting its practical application potential. This study highlights the application potential of preoxidized coal-tar-pitch-based carbon materials in high-performance SIB anodes. It provides a promising pathway for the high-efficiency utilization of industrial byproducts and the development of low-cost, high-performance energy storage systems. The findings offer valuable insights for advancing the development of SIB anode materials and optimizing the design of energy-storage electrodes.

Acknowledgements

None.

Author contribution statement

Yibo Zhao: Formal analysis, Resources, Methodology, Investigation, Data curation, Writing - original draft, Writing - review & editing, Validation. Peihua Li: Writing-review & editing, Validation, Methodology, Data curation. Rufeng Tian: Resources, Methodology, Investigation. Haochen Xie: Methodology, Formal analysis. Yalong Wang: Resources, Methodology, Investigation. Wanggang Zhang: Validation, Methodology. Xiaohong Li: Validation, Methodology. Jian Wang: Methodology, Formal analysis, Project administration, Funding acquisition, Writing - review & editing, Supervision. Yiming Liu: Formal analysis, Methodology, Funding acquisition, Project administration, Conceptualization, Supervision, Validation. All the authors have approved the final manuscript.

Data availability

The datasets generated during this study are fully available within the article and supplementary materials.

Declaration of competing interest

The authors declare that they have no known competing financial interests or personal relationships that could have appeared to influence the work reported in this paper.

Funding

The authors are grateful for the supporting from National Natural Science Foundation of China (Grant Nos. U25B201411, 22075197 and 22278290), the Shanxi Provincial Central Guidance Fund for Local Science and Technology Development Projects (Grant No. YDZJSX2024D022), and the Key Research and Development (R&D) Projects of Shanxi Province (Grant No. 202102040201003).

Use of AI statement

None.

Electronic Supplementary Material: Supplementary material is available in the online version of this article at https://doi.org/10.26599/EMD.2024.9370093

References

[1] Aslam, J., Waseem, M. A., Lu, X. M., Sun, W. W., Wang, Y. (2025). From biochar to battery electrodes: a pathway to green lithium and sodium-ion battery systems. *Chem. Eng. J.* 505, 159556.

[2] Begüm Yılmaz, E., Eren, E. O., Horner, T., Song, Z. H., Sheidaei, Y., Siewert, I., Senokos, E., Giusto, P. (2025). Reductive carbon materials: tailoring chemistry and electronic properties to improve sodium-ion batteries. *Angew. Chem. Int. Ed.* 64, e202422714.

[3] Lu, Z. X., Wang, J., Feng, W. L., Yin, X. P., Feng, X. C., Zhao, S. Y., Li, C. X., Wang, R. X., Huang, Q. A., Zhao, Y. F. (2023). Zinc single-atom-regulated hard carbons for high-rate and low-temperature sodium-ion batteries. *Adv. Mater.* 35, 2211461.

[4] Wu, X., Li, Z. X., Yin, T., Du, S. X., Zhang, C., Xiao, Z. H., Xu, Z. M., Li, Y. F. (2025). Molecular oxidative cross-linking engineering of low-cost pitch to hard carbon anodes for high-performance sodium-ion batteries. *ACS Sustainable Chem. Eng.* 13, 20522–20533.

[5] Jiang, Y., Xiao, N., Song, X. D., Xiao, J., Yu, K., Dai, X. H., Lv, Z. D., Qiu, J. S. (2024). Coal tar pitch derived sp^2 configuration-dominated vacancy-rich carbon with expand interlayer spacing for low-voltage, durable, and fast potassium storage. *Adv. Funct. Mater.* 34, 2316207.

[6] Zhang, Y. X., Han, B., Tan, S. S., Gao, Q., Cai, Z., Zhou, C. G., Li, J. T., Sun, R. M., Amine, K. (2025). Interfacial engineering of metal chalcogenides-based heterostructures for advanced sodium-ion batteries. *Adv. Energy Mater.* 15, 2404796.

[7] Xiao, Y., Miao, Y., Wan, S., Sun, Y. K., Chen, S. M. (2022). Synergistic engineering of Se vacancies and heterointerfaces in zinc-cobalt selenide anode for highly efficient Na-ion batteries. *Small* 18, 2202582.

[8] Qian, K. Y., Li, L., Yang, D. H., Wang, B. B., Wang, H., Yuan, G. H., Bai, J. T., Ma, S. H., Wang, G. (2023). Metal-electronegativity-induced, synchronously formed hetero- and vacancy-structures of selenide molybdenum for non-aqueous sodium-based dual-ion storage. *Adv. Funct. Mater.* 33, 2213009.

[9] Xu, J. C., Liang, H. H., Cai, J. B., Wang, J. L., Wu, J., Li, S. D., Yang, Z. H. (2023). Construction of ZnSe protective layer on zinc oxide for ultra-stable cycling of zinc-nickel batteries at high rates. *Chem. Eng. Sci.* 281, 119222.

[10] Chong, S. K., Ma, M., Yuan, L. L., Qiao, S. Y., Dong, S. H., Liu, H. K., Dou, S. X. (2023). Hierarchical encapsulation and rich sp^2 N assist Sb_2Se_3-based conversion-alloying anode for long-life sodium- and potassium-ion storage. *Energy Environ. Mater.* 6, e12458.

[11] Baqi, S., Oo, M. T., Ling, F. C. C. (2025). Unveiling the impact of Cu doping on charge carrier density and transfer in ZnO/ZnSe heterojunctions for PEC applications. *Mater. Sci. Semicond. Process.* 198, 109780.

[12] Zhu, J., Yang, Y., Zhao, Y. F., Lin, J. J., Zhang, J., Guo, P. Q., Wang, X. H. (2025). Toward dendrite-free and fast-charging lithium metal batteries: interfacial engineering of 3D ZnO/ZnSe heterostructural lithium hosts. *Sci. China Mater.* 68, 4068–4076.

[13] Li, X. Y., Han, Z. Y., Yang, W. H., Li, Q., Li, H. S., Xu, J., Li, H. L., Liu, B., Zhao, H. G., Li, S. D., et al. (2021). 3D ordered porous hybrid of ZnSe/*N*-doped carbon with anomalously high Na^+ mobility and ultrathin solid electrolyte interphase for sodium-ion batteries. *Adv. Funct. Mater.* 31, 2106194.

[14] Deng, Z. N., Jiang, H., Li, C. Z. (2018). 2D metal chalcogenides incorporated into carbon and their assembly for energy storage applications. *Small* 14, 1800148.

[15] Kumar, J., Solangi, N. H., Neiber, R. R., Bai, F. Y., Sharma, B. P., Charles, V., Zhai, P. F., Wang, Z. P., Yang, X. W. (2025). Chemical perspectives on synthesis, functionalization, artificial intelligence, and energy storage applications of layered double hydroxides-based nanomaterials: a comprehensive review. *Coord. Chem. Rev.* 537, 216705.

[16] Zhang, Y., Zhang, Y. R., Ma, L. Q., Yang, M., Zhao, X. Y. (2022). NiCr-Cl LDH/rGO composite as anode material for sodium-ion batteries. *J. Electron. Mater.* 51, 6067–6075.

[17] Tai, P. C., Chung, R. J., Wang, G. B., Kongvarhodom, C., Husain, S., Yougbaré, S., Chen, H. M., Wu, Y. F., Lin, L. Y. (2024). Polydopamine derived carbon coated cobalt molybdenum layered double hydroxide as highly stable anode materials of sodium-ion battery. *J. Energy Storage* 101, 113961.

[18] Li, Y. Z., Xu, C. X., Li, D. M., Zhang, Y. J., Ni, G. X., Xu, S. S., Liu, B., Huo, P. P. (2024). Sodium-ion batteries enabled by CoSn-LDH microspheres anchored on few-layer Ti_3C_2 MXene. *ACS Appl. Nano Mater.* 7, 20598–20608.

[19] Dong, X. F., Chen, F. J., Chen, G. G., Wang, B., Tian, X. L., Yan, X. L., Yin, Y. X., Deng, C. W., Wang, D., Mao, J. F., et al. (2022). NiS_2 nanodots on N,S-doped graphene synthesized via interlayer confinement for enhanced lithium-/sodium-ion storage. *J. Colloid Interface Sci.* 619, 359–368.

[20] Wang, J., Li, P. H., Chen, J. R., Xin, Y. C., Huangfu, C. H., Li, X. H., Zhang, W. G., Liu, Y. M. (2024). Innovative multielement modification of pitch-derived two-dimensional carbon nanosheets as anodes for superior performance sodium-ion batteries. *ACS Appl. Mater. Interfaces* 16, 60576–60587.

[21] Xu, R., Yi, Z. L., Song, M. X., Chen, J. P., Wei, X. X., Su, F. Y., Dai, L. Q., Sun, G. H., Yang, F., Xie, L. J., et al. (2023). Boosting sodium storage performance of hard carbons by regulating oxygen functionalities of the cross-linked asphalt precursor. *Carbon* 206, 94–104.

[22] Li, Y. L., Yuan, Z. Y., Li, D. D., Li, J. Z., Zhang, Y. M., Wang, M. R., Li, G. S., Wang, L. L., Han, W. (2024). Multi-interface combination of bimetallic selenide and $V_4C_3T_x$ MXene for high-rate and ultrastable sodium storage devices. *ACS Nano* 18, 4733–4745.

[23] Buttersack, C. (2019). Modeling of type IV and V sigmoidal adsorption isotherms. *Phys. Chem. Chem. Phys.* 21, 5614–5626.

[24] Zhang, J. H., Zhang, D. L., Li, K., Tian, Y. X., Wang, Y., Sun, T. (2021). N, O and S co-doped hierarchical porous carbon derived from a series of samara for lithium and sodium storage: insights into surface capacitance and inner diffusion. *J. Colloid Interface Sci.* 598, 250–259.

[25] Chen, C., Huang, Y., Meng, Z. Y., Xu, Z. P., Liu, P. B., Li, T. H. (2021). Multi-heteroatom doped porous carbon derived from insect feces for capacitance-enhanced sodium-ion storage. *J. Energy Chem.* 54, 482–492.

[26] Muruganantham, R., Wang, F. M., Liu, W. R. (2022). A green route N, S-doped hard carbon derived from fruit-peel biomass waste as an anode material for rechargeable sodium-ion storage applications. *Electrochim. Acta* 424, 140573.

[27] Gao, R., Zhang, T., Zhang, X. F., Gao, S., Xu, Y. M., Cheng, X. L., Gao, J. S., Zheng, M., Zhou, X., Huo, L. H. (2023). One-step controlled synthesis of ZnO-ZnSe hollow nanospheres with surface defects for selective detection of NO_2. *Appl. Surf. Sci.* 635, 157628.

[28] Luo, X., Shao, J., He, P., Li, K., Zhao, W. W. (2023). Construction of hierarchical ZnS/MoS_2 bimetallic sulfides heterostructures for high-performance sodium ion batteries. *Appl. Surf. Sci.* 607, 154821.

[29] Duraisamy, E., Prabunathan, P., Mani, G., Alshgari, R. A., Elumalai, P. (2021). [Zn(Salen)] metal complex-derived ZnO-implanted carbon slabs as anode material for lithium-ion and sodium-ion batteries. *Mater. Chem. Front.* 5, 3886–3896.

[30] Huang, Y. X., Wang, Z. H., Guan, M. R., Wu, F., Chen, R. J. (2020). Toward rapid-charging sodium-ion batteries using hybrid-phase molybdenum sulfide selenide-based anodes. *Adv. Mater.* 32, 2003534.

[31] Gao, Q., Li, P. C., Ding, S. S., He, H. C., Cai, M. Q., Ning, X. T., Cai, Y., Zhang, M. (2020). Cu_2Se-ZnSe heterojunction encapsulated in carbon fibers for high-capacity anodes of sodium-ion batteries. *Ionics* 26, 5525–5533.

[32] Iqbal, S., Wang, L., Kong, Z., Zhai, Y. J., Wang, F. B., Jing, Z. X., Sun, X. P., Wang, B., He, X. Y., Dou, J. M., et al. (2024). 2D Se-rich ZnSe/$CoSe_2$@C heterostructured composite as ultrastable anodes for alkaline-ion batteries. *Small* 20, 2404193.

[33] Guo, J. X., Zhao, Z. F., Xiong, Q. Q., Hu, X. S., Zhang, W., Qin, H. Y., Yuan, Y. J. (2025). Nano-sized ZnSe with nitrogen-doped carbon anchored on carbon nanotubes for enhanced lithium-ion and sodium-ion storage. *J. Electron. Mater.* 54, 1040–1053.

[34] Ma, C. R., Tang, X., Ben, H., Jiang, W., Shao, X. Y., Wang, G. X., Sun, B. (2025). Promoting reaction kinetics and boosting sodium storage capability via constructing stable heterostructures for sodium-ion batteries. *Adv. Funct. Mater.* 35, 2412879.

[35] Wang, Y. Y., Kang, W. P., Wei, X. F., Lu, X. Q., Sun, D. F. (2024). Seed-induced strategy for the construction of nitrogen-doped carbon coated $MoSe_2$/ZnSe-NC nanotubes with enriched phase boundaries toward boosting Na/K-ion storage. *Chem. Eng. J.* 482, 148927.

[36] Li, Z. Y., Zhang, D. Y., Xia, X., Yang, B., Li, Y. X., Yin, T. T., Wang, B., Wang, K. J., Cao, Y. Z. (2025). Heterojunctions based on (Co, Fe)Se_2 nanostructures on carbon nanotubes for rapid ion diffusion in sodium-ion batteries. *ACS Appl. Nano Mater.* 8, 1065–1077.

[37] Huang, H., Zhao, L. J., Zheng, Z. Q., Xie, D., Liu, P., Mai, Y., Cheng, F. L. (2023). Synergistic S-doped biomass carbon and N-doped carbon for construction of interlayer expanded MoS_2 core/shell nanospheres for potassium and sodium storage. *Electrochim. Acta* 461, 142626.

[38] Xiao, X. H., Duan, X. G., Song, Z. R., Deng, X. L., Deng, W. T., Hou, H. S., Zheng, R. J., Zou, G. Q., Ji, X. B. (2022). High-throughput production of cheap mineral-based heterostructures for high power sodium ion capacitors. *Adv. Funct. Mater.* 32, 2110476.

[39] Qiao, S. Y., Zhou, Q. W., Liu, H. K., Dou, S. X., Chong, S. K. (2024). Entropy and electronic structure modulation of a Prussian blue analogue cathode with suppressed phase evolution for potassium-ion batteries. *Nano Lett.* 24, 15167–15177.

[40] Zhang, G. F., Zhang, L. J., Ren, Q. J., Yan, L., Zhang, F. M., Lv, W. J., Shi, Z. Q. (2021). Tailoring a phenolic resin precursor by facile pre-oxidation tactics to realize a high-initial-coulombic-efficiency hard carbon anode for sodium-ion batteries. *ACS Appl. Mater. Interfaces* 13, 31650–31659.

[41] Bai, Y. L., Liu, Y. S., Ma, C., Wang, K. X., Chen, J. S. (2018). Neuron-inspired design of high-performance electrode materials for sodium-ion batteries. *ACS Nano* 12, 11503–11510.

[42] Xu, C., Chen, K. Y., Yang, J. H., Ma, G., Wang, Y., Zhou, Z. Z., Wu, Z. X., Che, S., Li, Z. C., Tu, Y. X., et al. (2024). Synergistic effect of holey graphene and $CoSe_2$-$NiSe_2$ heterostructure to enhance fast Na-ion transport. *Chem. Eng. J.* 498, 155353.

[43] Chen, J., Quattrocchi, E., Ciucci, F., Chen, Y. H. (2023). Charging processes in lithium-oxygen batteries unraveled through the lens of the distribution of relaxation times. *Chem* 9, 2267–2281.

[44] Xia, J. L., Yan, D., Guo, L. P., Dong, X. L., Li, W. C., Lu, A. H. (2020). Hard carbon nanosheets with uniform ultramicropores and accessible functional groups showing high realistic capacity and superior rate performance for sodium-ion storage. *Adv. Mater.* 32, 2000447.

[45] Godiya, C. B., Ren, Z. F., Minofar, B., Leiviskä, T. (2025). Cyclic sorption/regeneration of ion exchange resins and UV/sulfite treatment for complete perfluorooctane sulfonate removal. *Chem. Eng. J.* 522, 167008.

[46] Wang, Z. Z., Qiao, S. Y., Ma, M., Li, T., Liu, H. K., Dou, S. X., Chong, S. K. (2025). High-entropy conversion-alloying anode material for advanced potassium-ion batteries. *ACS Nano* 19, 15148–15160.

[47] Zhang, X. F., Yi, Z. L., Tian, Y. R., Xie, L. J., Su, F. Y., Wei, X. X., Chen, J. P., Chen, C. M. (2024). Insight into the effect of structural differences among pitch fractions on sodium storage performance of pitch-derived hard carbons. *Carbon* 226, 119165.

[48] Hu, J. W., Li, X. W., Liang, Q. Q., Xu, L., Ding, C. S., Liu, Y., Gao, Y. F. (2024). Optimization strategies of $Na_3V_2(PO_4)_3$ cathode materials for sodium-ion batteries. *Nano-Micro Lett.* 17, 33.